PHYSICAL REVIEW MATERIALS **8**, 124402 (2024)

Editors' Suggestion

Origins of background signal effects in all-metallic non-local spin valves

A. J. Wright,[1,*] D. Bromley,[1] J. Watts,[2,3] J. Ramberger,[3] B. Kaiser,[3] M. J. Erickson,[2,3]
P. A. Crowell,[2] C. Leighton,[3] and L. O'Brien[1,†]
[1]*Department of Physics, University of Liverpool, Liverpool L69 7ZE, United Kingdom*
[2]*School of Physics and Astronomy, University of Minnesota, Minnesota 55455, USA*
[3]*Department of Chemical Engineering and Materials Science, University of Minnesota, Minnesota 55455, USA*

(Received 9 August 2024; accepted 4 November 2024; published 3 December 2024)

The non-local spin valve (NLSV) is a useful device for studying spin transport at nanoscopic dimensions, with potential technological applications. Despite this appeal, background signals, unrelated to spin diffusion, often hinder the interpretation of spin signals in NLSVs and could compromise performance in future devices. In this paper, we comprehensively investigate these background signals in all-metallic NLSVs fabricated from a variety of ferromagnetic (FM; $Ni_{80}Fe_{20}$, Fe, Co) and nonmagnetic (NM; Al, Cu) metals. We demonstrate that a background signal emerges in AC measurements, with contributions from both current spreading and thermoelectric effects, with a complex dependence on both temperature and FM injector-detector separation. Despite the complexity of these dependencies, we demonstrate excellent agreement with three-dimensional finite-element modelling that accounts for current-spreading and thermoelectric effects, across a wide range of temperatures, FM separations, and FM/NM pairings. This approach additionally offers a means to estimate the Seebeck coefficients for the tested FM/NM pairings, providing further insight into the charge and heat flow in such nanoscopic spintronic devices.

DOI: 10.1103/PhysRevMaterials.8.124402

I. INTRODUCTION

The exploitation of spin transport phenomena in nanoscale devices as a route to low-power logic and memory devices has been the subject of intense interest. The ability to generate pure-spin currents using the non-local spin valve (NLSV) has established it as a useful tool for investigating such phenomena, free from spurious effects associated with charge transport [1–9]. Moreover, in all-metallic NLSVs, the lateral geometry can alleviate resistance-area product scaling issues [10], enabling potential applications in hard-disk-drive read heads [11–14] and all-spin logic devices [15,16]. Yet, despite the abundance of spin-transport research using NLSVs, there remains substantial uncertainty regarding the origins of their so-called "background" signals, which can impact device operation and have been the subject of recent investigation [17–21].

As a pertinent example, in the widely used spin diffusion model for all-metallic NLSVs [22], the measured non-local magnetoresistive signal should be exclusively a measure of spin accumulation. In practice, however, there is invariably a nonzero offset in these measurements, which has been previously demonstrated to arise from current-spreading and thermoelectric effects [9,18,19,23]. Such thermoelectric effects in NLSVs have been of considerable interest [24], with evidence of magnetothermoelectric effects [21], anomalous Nernst effects [20,25,26] and thermal injection of spin currents via the spin-dependent Seebeck effect [3,27]. Further understanding and careful control of these phenomena and thermal gradients in such nanoscale devices is necessary for their integration into industrial applications [11,12,28], particularly for potential exploitation of thermally generated pure spin currents [16,27,29,30].

Although current-spreading and thermoelectric effects are generally accepted as the origin of the background signals in NLSV measurements, the existing literature remains incomplete: studies have been mostly limited to NLSVs with single pairings of ferromagnetic (FM) and nonmagnetic (NM) materials (typically NiFe with Cu or Ag) and at fixed temperatures [3,18,26,29], despite evidence that the background signal is both strongly temperature and material dependent [17,21,31]. In this paper, we aim to address this gap in knowledge and understanding by comprehensively exploring the origin of the background signal throughout the entire phase space of temperature, material pairing, and NLSV dimensions, and then correlating experimental measurements with three-dimensional (3D) simulations of charge and heat transport. We are thus able to relate the functional forms of the background signal to the Seebeck coefficients of the FM/NM pairings and the resistivity of the NLSV channel. Importantly, we demonstrate the background signal to be sensitive to Peltier heating/cooling at the FM/NM interface, despite it being

---

[*] Present address: Blackett Laboratory, Imperial College London, London, UK.

[†] Contact author: lobrien@liverpool.ac.uk

significantly weaker than Joule heating. We then find excellent qualitative agreement between experimental measurements and simulations. By fitting current-spreading and thermoelectric components of the simulated background signal to the experimental data across the entire phase space simultaneously, we are also able to extract effective Seebeck coefficients for the nanowires forming our NLSVs, calculated through a constant scaling of temperature-dependent bulk or thin film coefficients taken from literature. In doing so, we not only confirm current-spreading and thermoelectric effects as responsible for the background signal in NLSVs, but also provide a useful tool for understanding these effects at the nanoscale and the thermoelectric properties of NLSV materials.

II. METHODS

Devices were fabricated on $\mathrm{Si/Si_3N_4}$ (200 nm) substrates using electron-beam lithography (Vistec EBPG5000+) on a polydimethylglutarimide (PMGI)/polymethyl methacrylate (PMMA) bilayer resist stack with thicknesses of 700 nm and 300 nm, respectively. FM and NM materials were deposited via ultrahigh vacuum electron beam evaporation, at an angle of 49° and 90° to the substrate, respectively, without breaking vacuum, to ensure electrically transparent interfaces [9,32–34] as explicitly verified by contact resistance measurements. The deposition system had a base pressure of 10^{-10} Torr, with the pressures during deposition being in the range 8×10^{-10} to 4×10^{-8} Torr. FM materials had a nominal purity of 99.95% and were deposited at a rate of 0.5 Å/s; NM materials had a nominal purity of 99.999% and were deposited at a rate of 1 Å/s. Film thicknesses were monitored using quartz crystal monitors, calibrated using x-ray reflectivity measurements of single thin films, and had typical values of $t_{\mathrm{FM}} = 16$ nm and $t_{\mathrm{NM}} = 150$–300 nm for FM and NM materials, respectively (specific NM thicknesses are indicated in the figures). Device dimensions were measured using scanning electron microscopy. Across the entire set of devices, typical NM channel widths were in the range $w_{\mathrm{NM}} = 100$–200 nm, and FM contact widths ranged from $w_{\mathrm{FM}} = 50$–150 nm, with FM separations $d = 150$–3000 nm. Measurements of spin transport and the associated background signal were performed using an AC technique with 13-Hz current excitation, and an amplitude of either 316 µA or 1 mA. The linear voltage response was measured and normalized by the injection current amplitude. NM resistivities were obtained by local four-terminal measurements on each device. Values for the FM resistivities were obtained from measurements of separate nanowires fabricated using similar lithographic and deposition processes.

Simulations of current spreading, Joule heating, and thermoelectric effects in NLSVs were performed using the FEniCS Finite Element Method package for solving partial differential Eqs. [35,36], via the Dolfin Python interface [37]. Simulations were run on the University of Liverpool High Throughput Computing service, HTCondor. Tetrahedral meshes of NLSVs were generated using dimensions measured from SEM, with sufficient mesh density to minimise errors resulting from the mesh geometry, but without significant expense in terms of computation time. Experimental results for the resistivity for each metal were used in the simulations, and a simple approximation for thermal conductivity, κ, was incorporated using the Wiedemann-Franz law, $\kappa\rho = LT$, where ρ is the resistivity at temperature T and $L = 2.44 \times 10^{-8} V^2 K^{-2}$ is the Lorenz number. (We note that violations of the Wiedemann-Franz law have been demonstrated in a variety of metallic thin films and nanowires, suppressing L [38–41], and that this may be a source of some uncertainty in the thermal conductivities used in our simulations.) Phenomenological fits of Seebeck coefficients taken from literature [42–46] were used, so that continuous values of the Seebeck coefficient could be implemented. Thin film values were used where possible (i.e., for Fe and $\mathrm{Ni_{80}Fe_{20}}$), and bulk values were used otherwise. For the $\mathrm{Si/Si_3N_4}$ substrate, an estimate of the T-dependent thermal conductivity of $\mathrm{Si_3N_4}$ was taken from literature (ranging from ∼0.1 to $3\ \mathrm{W\,m^{-1}\,K^{-1}}$) [47] and a constant value of $2000\ \mathrm{W\,m^{-1}\,K^{-1}}$ was taken for B-doped Si [48]. Cooling via an exchange gas was incorporated as a Neumann boundary condition in the simulations using Newton's cooling law, $\vec{q}_{ex} \cdot \hat{n} = h(T' - T)$, where $\hat{n}$ is the surface normal, $T' - T$ is the temperature differential across the boundary, and $h = 100\ \mathrm{W\,m^{-2}\,K^{-1}}$ is the (T-independent) heat transfer coefficient for a helium exchange gas [49]. The rear surface of the Si substrate was fixed at T. DC currents in the simulations were injected from $\mathrm{FM_{inj}}$ and extracted from the far left of the NM channel of the NLSVs, held at 0 V. The non-local voltage was determined by finding the difference between the average voltage across the cross-sectional facets of the $\mathrm{FM_{det}}$ and the far-right of the NM channel. Voltages were divided by the injection current (1 mA, except where stated otherwise) in order to normalize effects that are linear with current (the focus of this paper). Current spreading effects were exclusively modelled by "turning off" heat-transport-related terms in the simulation; Peltier and Joule heating contributions (manifest as voltages via the Seebeck effect) were isolated by individually restoring those terms in the simulations and subtracting the current-spreading contribution.

III. RESULTS AND DISCUSSION

The NLSV geometry is shown in Fig. 1(a) and consists of an NM channel contacted by two FM wires, separated by a distance d. A charge current injected from the left FM contact ($\mathrm{FM_{inj}}$) into the NM channel becomes spin-polarized, generating a nonequilibrium spin accumulation in the NM. Spins then diffuse through the NM channel in the form of a pure spin current, which decays on a characteristic length scale λ_N, the spin-diffusion length [1,50]. The resulting spin accumulation at the second FM contact ($\mathrm{FM_{det}}$) generates a non-local voltage V_{NL}, between $\mathrm{FM_{det}}$ and NM, which is typically normalized to the injection current I_C, giving the non-local transimpedance $R_{\mathrm{NL}} = V_{\mathrm{NL}}/I_C$. In practice, however, a nonzero, spin-independent background R_b is present in such measurements—the aforementioned background signal [18,19,23]. The spin signal is therefore isolated by toggling the magnetization of the FMs between the parallel (P) and antiparallel (AP) states, yielding $\Delta R_{\mathrm{NL}} = R^P_{\mathrm{NL}} - R^{\mathrm{AP}}_{\mathrm{NL}}$. Such a measurement is shown in Fig. 1(b) for an Fe/Al NLSV with R^P_{NL}, $R^{\mathrm{AP}}_{\mathrm{NL}}$, and ΔR_{NL} indicated. The nonzero background resistance $R_b = (R^P_{\mathrm{NL}} + R^{\mathrm{AP}}_{\mathrm{NL}})/2$ is also shown in Fig. 1(b) and is clearly substantial relative to ΔR_{NL}.

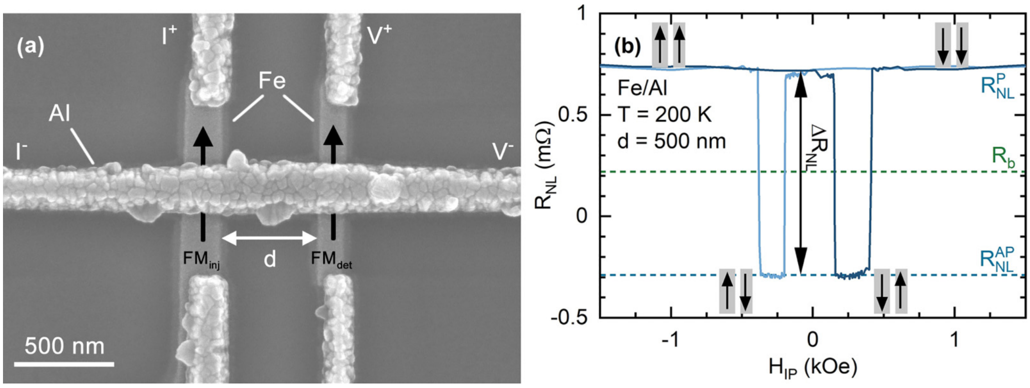

FIG. 1. (a) SEM image of an Fe/Al NLSV with $d = 500$ nm. The black arrows indicate the relative magnetization direction of the $\mathrm{FM}_{\mathrm{inj}}$ and $\mathrm{FM}_{\mathrm{det}}$. Note that the substantial edge roughness is a feature of Al-based devices only. (b) Example measurement of R_{NL} vs an in-plane magnetic field. The parallel and antiparallel states are indicated by the black arrows. The spin-signal ΔR_{NL} and non-local background R_b are shown on the figure.

The form and magnitude of R_b can reasonably be expected to be influenced by the choice of FM and NM materials, via their thermoelectric properties, and typically exhibits strong T dependence. The substrate also plays a role in thermal sinking of any heat generation [19,20]. In Fig. 2, experimental measurements of the background resistance are shown as a function of T for various pairings of FM and NM materials (on the same substrate), with comparable $d = 220$ or 250 nm and $t_{\mathrm{NM}} = 150$ or 200 nm. [We label these data as $R_{b,1}^{\mathrm{exp}}$, where the subscript "1" is used to denote the linear response of R_b to the injection current ($\propto I_C^1$) as measured in AC techniques, and the superscript "*exp*" explicitly distinguishes experimental measurements from the simulations discussed below.] The impact of the choice of both the FM and NM material is readily apparent in Fig. 2, affecting the magnitude and the form of $R_b(T)$, and even its sign. The $\mathrm{Ni}_{80}\mathrm{Fe}_{20}$/NM and Co/NM devices exhibit an apparently exponential-like increase with T, whereas the Fe/NM devices have an inflection point in $R_b(T)$, appearing to plateau at higher T. Further, the dependence on the NM materials appears variable also, with Cu producing a stronger response than Al in the Co and $\mathrm{Ni}_{80}\mathrm{Fe}_{20}$ devices, but a weaker response in the Fe devices.

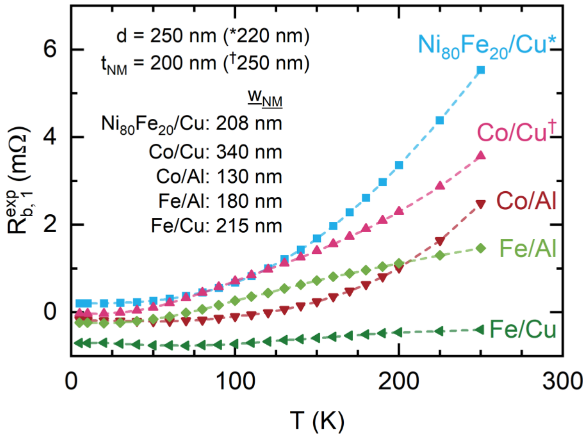

FIG. 2. The measured NLSV background resistance $R_{b,1}^{\mathrm{exp}}(T)$ for various pairings of FM/NM materials. There is a clear temperature dependence of $R_{b,1}^{\mathrm{exp}}$ that varies in magnitude and form for different FM/NM pairings. $d = 250$ nm and $t_{\mathrm{NM}} = 200$ nm for all devices, except those indicated by an asterisk or dagger, which have $d = 250$ nm or $t_{\mathrm{NM}} = 250$ nm, respectively. Across the entire set of devices, average NM widths are $\mathrm{Ni}_{80}\mathrm{Fe}_{20}$/Cu, 210 ± 20 nm; Co/Cu, 250 ± 50 nm; Co/Al, 150 ± 20 nm; Fe/Al, 160 ± 20 nm; and Fe/Cu, 200 ± 40 nm.

To better understand these data, we first focus on a single FM/NM pairing. Experimental measurements of $R_{b,1}^{\mathrm{exp}}(T)$ in Co/Al NLSVs (Al channel thickness $t_{Al} = 150$ nm) are shown by the data points in Fig. 3(a) for different d. Qualitatively, the monotonic increase of $R_{b,1}^{\mathrm{exp}}$ with increasing T, and exponential decay with increasing d are consistent with expectations from current spreading and thermoelectric effects. To a first-order approximation, current spreading (CS) effects give a contribution to $R_{b,1}^{\mathrm{exp}}$ of the form

$$R_{b,\mathrm{CS}} = \frac{\rho_{\mathrm{NM}}}{\pi t_{\mathrm{NM}}} \exp\left(-\frac{\pi d}{w_{\mathrm{NM}}}\right), \tag{1}$$

where ρ_{NM}, t_{NM}, and w_{NM} are the NM channel resistivity, thickness, and width, respectively [23]. This expression remains valid when the injector and detector are on the same side of the NM channel; when on opposite sides, Eq. (1) becomes negative. In addition, a one-dimensional (1D) model of thermal diffusion (TD) through the NM channel gives

$$R_{b,TD} \propto -S_{FM_{det}\text{-}NM}\, \Delta T_{inj} \exp\left(-d/\xi\right), \tag{2}$$

where ΔT_{inj} is the temperature difference between the $\mathrm{FM}_{\mathrm{inj}}$/NM interface and the far-right of the NM channel (assumed to be at the reference temperature T), and the factor ξ is a characteristic decay length, comprising parameters describing heat sinking to the substrate and the thermal conductivity of the channel [31]. $S_{FM_{det}\text{-}NM}$ is the relative Seebeck coefficient of the $\mathrm{FM}_{\mathrm{det}}$/NM pairing, which, in the idealized case, is simply the difference between the Seebeck coefficients of the two materials. The sign of $R_{b,TD}$ depends on $S_{FM\text{-}NM}$ and ΔT_{inj}, both of which can either be positive or negative: $S_{FM\text{-}NM}$ depends on the choice of the Seebeck coefficients of the $\mathrm{FM}_{\mathrm{det}}$ and NM materials (which can be positive or negative) and ΔT_{inj} depends on the source of temperature change, e.g., Joule heating or Peltier heating/cooling. Thus,

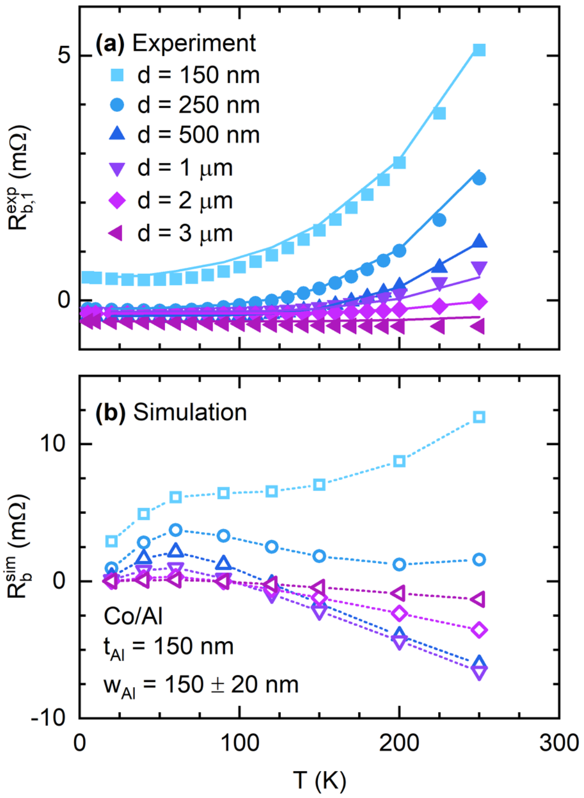

FIG. 3. (a) $R_{b,1}^{\rm exp}$ in Co/Al NLSVs for various d compared with (b) the simulation results $R_b^{\rm sim}$ including Peltier, Seebeck, and Joule heating terms. There is clearly a mismatch between $R_{b,1}^{\rm exp}$ and $R_b^{\rm sim}$ in both form and magnitude, because of the AC measurement of $R_{b,1}^{\rm exp}$ and the DC nature of the simulations for $R_b^{\rm sim}$. Solid lines in (a) are fits to the experimental data using the simulation results. Dotted lines in (b) are a guide to the eye.

R_b can be positive or negative and can, in principle, change sign with T.

Based on Eqs. (1) and (2), $R_b(d)$ is then essentially the linear combination of two exponential decays. However, these models are unable to describe the experimental data because of two key limitations. First, Eq. (1) assumes that the electronic mean-free-path $\lambda_e \gg t_{NM}$, reducing the system to 2D [23], which is not the case in our devices (where $\lambda_e \sim 10$ nm, compared with $t_N = 100$–300 nm). This model, therefore, does not properly capture the magnitude nor geometrical dependence of the current-spreading contribution to R_b. However, the general form of the exponential decay with d holds. Second, in the 1D thermal diffusion model of Eq. (2) [31], heat generation and heat losses to the substrate are poorly defined, and hence so are ΔT_{inj} and ξ, and the model cannot be properly constrained. Other studies have overcome this issue by fabricating devices on suspended membranes or thermal isolation platforms, to nullify thermal conduction to the substrate [20,27]. Instead, here we take a more general approach by modelling R_b using 3D finite-element method (FEM) simulations.

First, the necessary equations governing charge and heat transport must be defined. Charge and heat current densities, $\vec{j}$ and $\vec{q}$, respectively, are related to (spatially varying) voltage V and T gradients by a 6×6 matrix. Assuming isotropic material properties and ignoring magneto-thermoelectric and Hall effects (discussed later), this may be simplified to a 2×2 matrix, and hence

$$\begin{pmatrix} \vec{j} \\ \vec{q} \end{pmatrix} = -\begin{pmatrix} \sigma & \sigma S \\ \sigma \Pi & \kappa \end{pmatrix} \begin{pmatrix} \nabla V \\ \nabla T \end{pmatrix}, \tag{3}$$

where $\sigma (\equiv 1/\rho)$ and κ are the charge and thermal conductivities, respectively, S is the Seebeck coefficient and Π is the Peltier coefficient. The diagonal terms in the simplified 2×2 matrix are the ordinary Ohm's law and thermal conduction relations, while the off-diagonal terms encapsulate the Seebeck and Peltier effects. Introducing charge and heat continuity and Joule heating, Eq. (3) becomes

$$\nabla \cdot \vec{j} = -\sigma(\nabla^2 V + S\nabla^2 T) = 0, \tag{4a}$$

$$\nabla \cdot \vec{q} = -\sigma \Pi \nabla^2 V - \kappa \nabla^2 T = |\vec{j}|^2/\sigma. \tag{4b}$$

From Onsager reciprocity, the Peltier coefficient is given by $\Pi = ST$. For computational efficiency, we use the reference temperature of the measurement for T. Local temperature variations are expected to be on the order of a few Kelvin, at most, [31] and therefore we expect any errors from this approximation to be small. Simulations of charge and heat transport in NLSVs were performed using Eq. (4) for DC current injection. Since experimental measurements were of the first harmonic response to AC excitation currents, we ignore spin-dependent Seebeck effects [3,27,51] which do not appear in the first harmonic (they do, however, appear in DC and higher harmonic measurements [3,27]). Further, for the device dimensions considered here, we find no evidence of magnetothermoelectric effects [21] nor anomalous Nernst effects, which manifest as an asymmetry in $R_{\rm NL}(H)$ measurements [20,25] (although these do occur in devices with a thinner NM channel [21]). The 3D FEM approach does not implement interface thermal impedances [52,53]; while these effects will undoubtedly be present, we do not expect them to dominate in our measurements [24]. Neither can this approach account for thermal transport from (quasi)ballistic phonons [24,54–56], which is expected to be relevant at the low T and small length-scales here, although we do not observe evidence of this in our experimental measurements [31]. Despite these limitations, we find our model is able to reproduce experimental observations well, as demonstrated below.

The non-local background from the simulation $R_b^{\rm sim}$ is shown in Fig. 3(b) for meshes based on the devices measured in Fig. 3(a). Clearly, the simulation and experiment do not match in either T dependence or magnitude. This can be simply explained by the measurement configuration: The experimental first harmonic AC technique measures only the linear component of $R_b(I_C)$, whereas the simulations are performed for DC injection. For meaningful comparison between the two, the current-bias dependence of $V_b^{\rm sim}$ must therefore be understood. Nonlinear dependencies of $V_b^{\rm sim}$ on I_C can be expressed as a power series in I_C,

$$V_b^{\rm sim} = a_1 I_C + a_2 I_C{}^2 + a_3 I_C{}^3 + \cdots \tag{5}$$

where a_i is the coefficient of the ith harmonic response of the current I_C. Simulations of the devices were performed across bias currents ranging from -1 to $+1$ mA, and the $V_b^{\rm sim}(I_C)$ data were fit to a cubic function (higher-order terms were

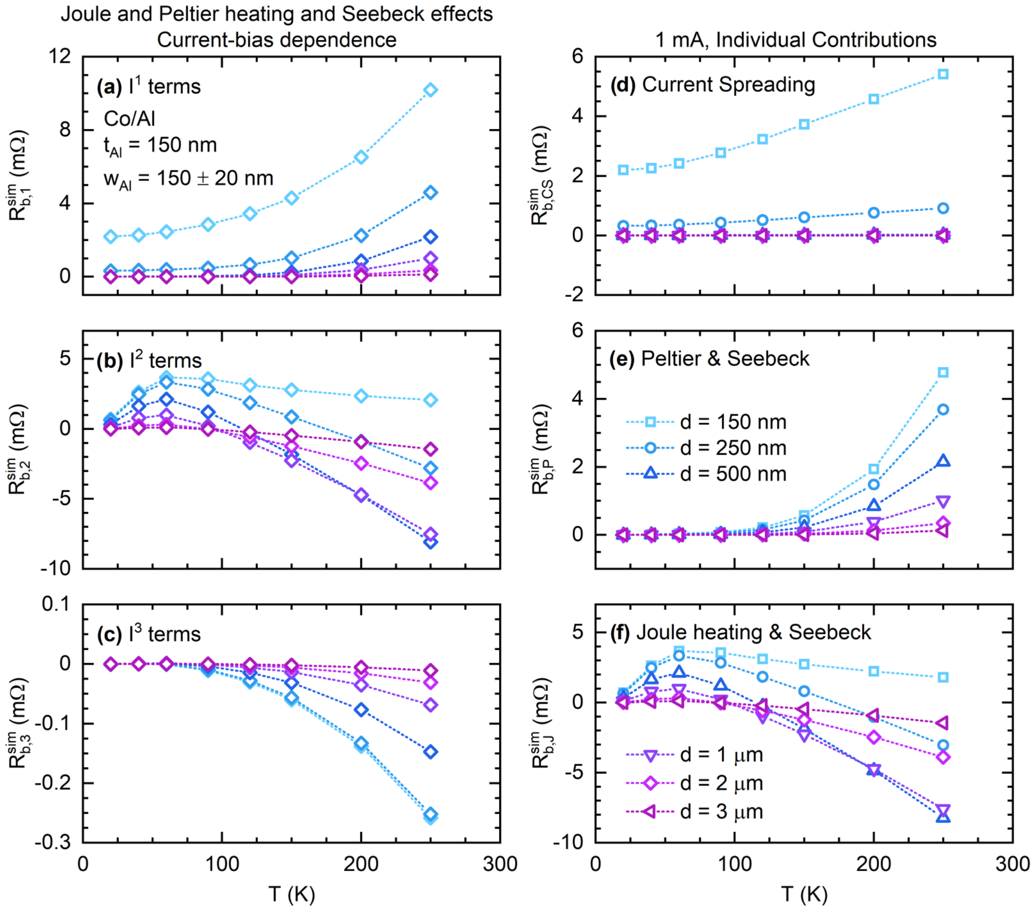

FIG. 4. Current bias dependence of R_b^{sim} in Co/Al devices, shown for the (a) linear, (b) quadratic, and (c) cubic responses to I_C, including current spreading, Joule heating, Peltier heating, and Seebeck effects. Individual contributions of (d) current spreading, (e) Peltier, and (f) Joule heating effects. By comparison, current spreading and Peltier effects are subsumed in $R_{b,1}^{\mathrm{sim}}$, and Joule heating in $R_{b,2}^{\mathrm{sim}}$. Device dimensions used are the same as in Fig. 3. Dotted lines are a guide to the eye.

found negligible). The T and d dependencies of the components a_i from the fits are shown in Figs. 4(a)–4(c), normalized to an injection current of $I_C = 1$ mA, i.e., $R_{b,1}^{\mathrm{sim}} = a_1$, $R_{b,2}^{\mathrm{sim}} = a_2 I_C$, and $R_{b,3}^{\mathrm{sim}} = a_3 I_C^2$. Also shown in Figs. 4(d)–4(f) are the individual contributions to R_b^{sim} from current spreading, Peltier, and Joule heating effects, indicated by the subscripts CS, P, and J, respectively.

Current spreading effects [Fig. 4(d)] are directly proportional to ρ_{NM}, decaying exponentially with d, as expected from Eq. (1), although the exact magnitude and rate of decay in the simulations differ from the model. Peltier contributions, too, are expected to depend exponentially on d, because of heat generation at the $\mathrm{FM_{inj}}/\mathrm{NM}$ interface that is conducted through the NM channel; indeed $R_{b,P}^{\mathrm{sim}}(T, d)$ [Fig. 4(e)] follows this form closely (see Appendix A). Joule heating effects [Fig. 4(f)] are more complex. Heat is primarily generated in the $\mathrm{FM_{inj}}$ owing to its typically high ρ, producing an exponential dependence on d (following similar arguments to the Peltier contribution), as observed in Fig. 4(f) for $d \geqslant 1$ μm. At short d, however, lateral thermal conduction through the substrate heats $\mathrm{FM_{det}}$, producing competing T dependencies, and hence the complex form of $R_{b,J}^{\mathrm{sim}}(T)$ for $d \leqslant 500$ nm.

Comparing now the power series components of $R_b^{\mathrm{sim}}(I_C)$ [Fig. 4(a)–4(c)] with the individual contributions [Figs. 4(d)–4(f)], it is clear that the $I_C{}^1$ component is dominated by current-spreading and Peltier effects, whereas the $I_C{}^2$ component exactly follows the Joule heating contribution. We also observe an $I_C{}^3$ dependence that appears to be a mix of the Peltier and Joule heating effects [18], but is orders of magnitude weaker than the $I_C{}^1$ and $I_C{}^2$ components and is hence negligible. As a result, we conclude that DC simulations of current spreading and Peltier effects can be used as an unambiguous proxy for a linear response model with coefficient R_b and hence of first harmonic experimental AC measurements.

Returning to the experimental measurements of R_b^{exp} in Fig. 3(a), we observe excellent agreement with the simulation results in Fig. 4(a), albeit with a factor of ∼2 difference in the magnitudes of $R_{b,1}$. Such a discrepancy is reasonable given that the magnitude of the current-spreading effects is sensitive to the exact geometry of current injection and detection [23], which we can only approximate with the simulated mesh. Additionally, the varying literature measurements of thin film Seebeck coefficients will undoubtedly introduce discrepancies: Seebeck coefficients are sensitive to the dominant momentum scattering mechanisms present in a given material [57], and therefore changes in ρ, e.g., through enhanced surface relaxation, will produce different coefficients.

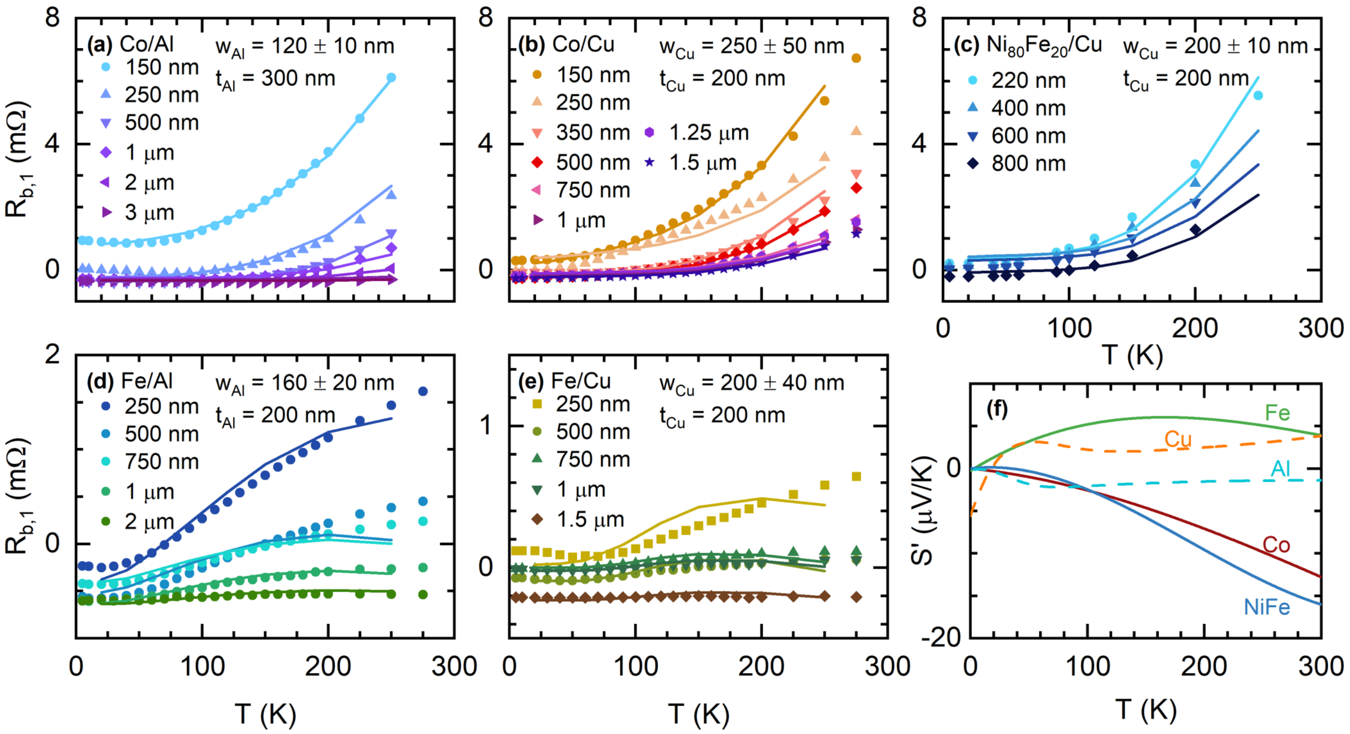

FIG. 5. Experimental measurements of $R_{b,1}$ in NLSVs with various FM/NM pairings, and simulation data fit to the experimental data using Eq. (6) (solid lines). (a) Co/Al ($t_{\mathrm{NM}} = 300$ nm), (b) Co/Cu, (c) $\mathrm{Ni_{80}Fe_{20}/Cu}$, (d) Fe/Al, and (e) Fe/Cu. (f) Scaled absolute Seebeck coefficients for the FM and NM materials obtained from fitting the data in panels (a)−(e) with literature values [42–46], demonstrating self-consistency of the model. Solid lines are used for FM materials and dashed lines for NM materials.

Accepting these shortcomings, but assuming the T and d dependencies to be correct, the simulation data can be fit to the experimental data as a linear, scaled combination of the current-spreading and Peltier contributions,

$$R_{b,1}^{\mathrm{exp}}(d,T) = c_{\mathrm{CS}} R_{b,\mathrm{CS}}^{\mathrm{sim}}(d,T) + c_P R_{b,P}^{\mathrm{sim}}(d,T) + R_0(d). \quad (6)$$

Here, c_{CS} and c_P are constant coefficients, independent of d and T. $R_0(d)$ is a T-independent term, which accounts for any finite offset voltages related to the measurement setup and unrelated to the sample under test [58]. The resulting fits for the Co/Al data are shown by the solid lines in Fig. 3(a), reproducing the experimental data very closely. The fits return $c_{\mathrm{CS}} = 0.45$ for current spreading (reasonable given the arguments above), and $c_P = 0.69$, which can be understood as a scaling of the *relative* Seebeck coefficient for this Co/Al system by the same factor [see Eq. (7) of Appendix A].

Encouraged by this, we proceed to simulate R_b in devices with different FM/NM pairings. Experimental data for Co/Al with a thicker Al channel ($t_{Al} = 300$ nm), and Co/Cu, $\mathrm{Ni_{80}Fe_{20}/Cu}$, Fe/Al and Fe/Cu (all with $t_{\mathrm{NM}} = 200$ nm) are shown in Figs. 5(a)–5(e). Given the range of FM/NM pairings available to us, we explore whether we can extract *absolute* Seebeck coefficients for each material and check whether they are consistent with the values that were originally assumed based on the literature. Assuming that the T dependence of the Seebeck coefficients remains unchanged from the literature bulk/thin film values, but that the magnitude changes, we replace the Peltier scaling parameter c_P in Eq. (6) with the factor $[S'_{FM\text{-}NM}(T)/S_{FM\text{-}NM}(T)]^2$ where $S'_{FM\text{-}NM}(T) = c_P^{\mathrm{FM}} S_{\mathrm{FM}}(T) - c_P^{\mathrm{NM}} S_{\mathrm{NM}}(T)$, and c_P^{FM} and c_P^{NM} are individual scaling factors for the FM and NM Seebeck coefficients respectively (see Appendix A). We then proceed to fit the simulation data to the experimental results, employing c_P^{FM} and c_P^{NM} as single-valued, free parameters, simultaneously fit across the entire dataset. A weak background, linear with T, has been subtracted from the data; we observe this background to be independent of d, t_{NM}, and material pairing and interpret it to be an artefact of the measurement geometry.

The results from the fits are shown by the solid lines in Figs. 5(a)–5(e), and the extracted effective Seebeck coefficients are presented in Fig. 5(f). Across most of the data, the fits reproduce the experimental data exceptionally well, and, reassuringly, all Seebeck scaling parameters c_P^{FM} and c_P^{NM} are within a range 0.8–2.2. The exponential-like increase with T in $R_{b,1}$ across the Co/Al, Co/Cu, and $\mathrm{Ni_{80}Fe_{20}/Cu}$ devices are all well reproduced by the fits, suggesting that the T dependences of the Seebeck coefficients for these materials are correct. The fits to the Fe/Al data are also reasonable, showing the onset of a high-T plateau, although the temperature at which this occurs is somewhat inconsistent between simulations and experimental measurements. Further, in the Fe/Cu data, the simulations fail to properly capture the undulating form of $R_{b,1}^{\mathrm{exp}}$, indicating that the peak in S_{Fe} occurs at a higher T in our devices than in the literature values for bulk Fe that we have used. In Appendix B, we describe an approach in which we are able to estimate S_{Fe}, by applying a simple model to the simulation results to capture the dependence of $R_{b,1}$ on $S_{FM\text{-}NM}$. Applying this to the experimental Fe/Cu data, we extract data for $S_{Fe}(T)$, which exhibits the shifted temperature peak indicated by the $R_{b,1}^{\mathrm{exp}}$ data.

The excellent quantitative agreement between the experimental measurements and simulations in this paper, across a comprehensive range of T and material pairings, is clear evidence that the background signal observed in NLSV measurements originates from current-spreading and thermoelectric effects. This comprehensive phase space has not been previously explored; in doing so here we have been able to test the validity of the current-spreading and thermoelectric contributions. In particular, we observe that the characteristic exponential-like increase of $R_{b,1}^{\exp}$ with T is not universal to all FM/NM pairings but is instead sensitive to the choice of both materials. Despite this, we naturally obtain the unusual form of $R_{b,1}^{\exp}$ in Fe/Al and Fe/Cu with ordinary current-spreading and thermoelectric models. Further, at small d in these electrically transparent interface devices, current spreading is comparable in magnitude to the thermoelectric background, and the complex interplay between the two contributions is explicitly necessary to explain the full background signal. At larger d, current spreading falls off quickly, and the background signal is dominated by the thermoelectric contribution.

The permutations of different material pairings probed here provide another key advantage in allowing us to extract absolute Seebeck coefficients for the individual materials. This reveals self-consistency with the T dependence of Seebeck coefficients in the literature, although we observe different magnitudes. This discrepancy is readily explained by differences in the resistivities of the materials and the specific contributions to ρ, e.g., enhanced grain boundary or surface scattering in nanowires as compared to bulk materials [57]. The methods in this paper thus provide a useful tool to understand the background signal in NLSV measurements, as well as the thermoelectric properties of the device materials that contribute to it. Furthermore, by adopting a measurement geometry in which $\mathrm{FM_{inj}}$ acts exclusively as a thermal spin-current injector [3,27,29], the method developed here could feasibly be extended to probe spin-dependent Seebeck coefficients in an array of materials. We note that there may be additional features at lower T that we do not explore here. Specifically, there is speculation that, in material pairings where the NM can host magnetic impurity moments from the FM (i.e., Kondo-active pairings), there is expected to be an additional, substantial term in the NM Seebeck coefficient arising from the Kondo giant thermopower [59–63] and we suspect it is present in the Fe/Cu data in this work [see Figs. 2 and 5(e)], although we lack statistical certainty.

In technological applications of NLSVs, e.g., spin accumulation sensors for magnetic recording [11,13], the impact of background signals remains unclear. Device thicknesses are expected to be on the order of a few nm to achieve ultrahigh-density and large output signals [11,12,14]. As the NM cross-sectional area shrinks, current-spreading and thermal transport in the NM channel are expected to decrease [23,31] [see, for example, the reduction in $R_{b,1}^{\exp}$ from $t_{Al} = 300$ nm to 150 nm in Figs. 5(a) and 3(a), respectively]. In contrast, a smaller FM cross section will lead to increased Joule heating, relevant for DC applications, further compounded by reduced heat sinking in the absence of a large substrate (although this may be mitigated by the inclusion of FM shields, which would provide additional heat sinks). Additionally, thermoelectric effects are typically strongest at the relevant temperatures for these applications, i.e., room temperature, [42–46] and shorter channel lengths will exponentially increase the strength of the current-spreading and thermoelectric backgrounds [23,31]. A deeper understanding of the impact of these effects on signal fidelity in these regimes will therefore be important for device design in these applications.

In summary, we have comprehensively demonstrated strong agreement between experimental measurements of R_b in NLSVs and theoretical simulations based on current-spreading and Peltier effects, across a large range of T, d, and FM/NM pairings. Finite-element method simulations reveal the sensitivity of AC measurements to Peltier heating, despite Joule heating being the dominant heating mechanism. Through simultaneous fitting across our entire data set, our simulation data are able to accurately reproduce the experimental measurements, even the seemingly complex behavior of $R_{b,1}^{\exp}(T)$ in Fe/Al and Fe/Cu devices, which has not been previously reported.

ACKNOWLEDGMENTS

Work at the University of Liverpool was supported by the UK EPSRC, Grant No. EP/P005713/1. Work at the University of Minnesota (UMN) was supported by the National Science Foundation under Award No. DMR-2103711, ASRC, and Seagate Technology Inc.. Parts of this work were performed in the Characterization Facility, UMN, and the Minnesota Nano Center, which receive support from NSF through the MSREC program and National Nano Coordinated Infrastructure Network (Awards No. DMR-2011401 and No. ECCS-2025124, respectively). We thank Dr. Ian Smith for assistance using the University of Liverpool HTCondor system. We also thank Barry Zink for useful discussions.

APPENDIX A: EXPONENTIAL BEHAVIOR OF PELTIER HEATING

Peltier heating/cooling at the $\mathrm{FM_{inj}}$/NM interface generates a temperature gradient in the NM channel that, according to the 1D heat diffusion model of Eq. (2), decays exponentially as heat is sunk to the substrate: $\partial T/\partial x \propto I_C \Pi_{FM\text{-}NM} \exp(-x/\xi)$, where x is the distance from the $\mathrm{FM_{inj}}$/NM interface [31]. Here, $\Pi_{FM\text{-}NM} \equiv \Pi_{\mathrm{FM}} - \Pi_{\mathrm{NM}}$ is the relative Peltier coefficient of the FM and NM materials. This temperature gradient generates a corresponding potential difference between $\mathrm{FM_{det}}$ and the far right of the NM channel given by

$$V_P \propto S_{FM\text{-}NM} \Delta T \propto I_C T S_{FM\text{-}NM}^2 \exp\left(-d/\xi\right), \qquad (7)$$

where ΔT is the temperature difference between $\mathrm{FM_{det}}$ and the far right of the NM channel (assumed to be at temperature T) and we have used the definition $\Pi_{FM-NM} = T S_{FM-NM}$ ($S_{FM-NM} \equiv S_{\mathrm{FM}} - S_{\mathrm{NM}}$ is the relative Seebeck coefficient of the NM and FM materials). Hence, the Peltier and Seebeck contributions to R_b should follow $T S_{FM\text{-}NM}^2$ and decay exponentially with d.

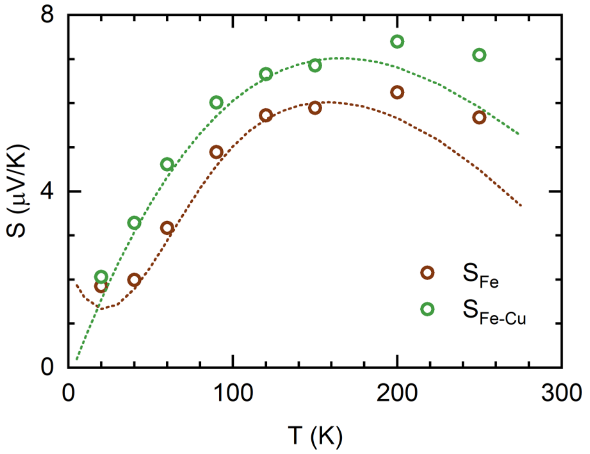

FIG. 6. Estimated relative Seebeck coefficient for Fe/Cu and absolute Seebeck coefficient for Fe from exponential fits to simulations and experimental data (circles), compared with literature values [43,44] (dashed line).

APPENDIX B: EXTRACTING $S_{\text{Fe-Cu}}$ AND S_{Fe}

Both contributions to $R_{b,1}$, i.e., current-spreading and Peltier effects, are expected to be exponentially dependent on d see Eqs. (2) and (7) and indeed simulations of these effects reveal this trend. Hence, it should be possible to express $R_{b,1}$ at a given T as a sum of two exponential terms. As a further simplification, current-spreading effects have a much faster fall off than Peltier effects [compare, for example, the d dependenies of $R_{b,\text{CS}}$ and $R_{b,P}$ in Figs. 4(d) and 4(e)]. Therefore, at sufficiently high d, $R_{b,1}$ may be simply expressed as

$$R_{b,1} = B\exp\left(-d/\xi\right), \tag{8}$$

at fixed T, where the amplitude $B = AS^2_{FM-NM}$, and A is some scaling factor that captures ρ, κ and the device geometry. Using Eq. (8) to fit the Fe/Cu $R^{\text{sim}}_{b,1}(d)$ data at different T, where $d \geqslant 750$ nm (sufficiently high for current-spreading to be negligible), we obtain values for $A(T)$, by dividing the extracted $B(T)$ data by the literature $S_{\text{Fe-Cu}}$ values used in the simulations. Since device dimensions and ρ are experimentally measured values, from which the relevant κ is estimated, and $A(T)$ is derived from these quantities, we may assume these $A(T)$ values hold for our experimental measurements. Fitting the experimental Fe/Cu data in the same way yields amplitudes $B^{\text{exp}}(T)$, from which we can extract experimental $S_{\text{Fe-Cu}}(T)$ values using the previously obtained $A(T)$ from fitting the simulation data.

The $S_{\text{Fe-Cu}}(T)$ data obtained using this method are shown by the circles in Fig. 6(a) and compared with the (bulk/thin film) literature values (dashed line) [43,57]. At low $T (\leqslant 150$ K) there is excellent agreement between the extracted $S_{\text{Fe-Cu}}$ data and the literature values. Above 150 K, there is some divergence, with the high-T downturn being pushed to higher temperatures in the extracted values, as implied by the observations in Fig. 5(e). Since similar behavior is observed in the Fe/Al data, we reason that this divergence is due to a change in the Fe Seebeck coefficient. Assuming that S_{Cu} is unchanged, we may accordingly estimate S_{Fe}, as shown in Fig. 6(b), again compared with the literature values. In doing so, we observe the peak in S_{Fe} is pulled to lower T. This peak arises from magnon drag [44] and is reasonably expected to differ between bulk, thin films, and nanowires, as damping, magnon lifetimes, and the effect of defects and impurities vary [64,65]. Accounting for such effects is difficult, yet by combining our experimental measurements with simulations we are able to estimate the resulting change in S_{Fe}.

---

[1] F. J. Jedema, A. T. Filip, and B. J. van Wees, Electrical spin injection and accumulation at room temperature in an all-metal mesoscopic spin valve, Nature (London) **410**, 345 (2001).

[2] J. D. Watts, J. T. Batley, N. A. Rabideau, J. P. Hoch, L. O'Brien, P. A. Crowell, and C. Leighton, Finite-size effect in phonon-induced Elliott-Yafet spin relaxation in Al, Phys. Rev. Lett. **128**, 207201 (2022).

[3] M. Erekhinsky, F. Casanova, I. K. Schuller, and A. Sharoni, Spin-dependent Seebeck effect in non-local spin valve devices, Appl. Phys. Lett. **100**, 212401 (2012).

[4] M. Erekhinsky, A. Sharoni, F. Casanova, and I. K. Schuller, Surface enhanced spin-flip scattering in lateral spin valves, Appl. Phys. Lett. **96**, 022513 (2010).

[5] F. Casanova, A. Sharoni, M. Erekhinsky, and I. K. Schuller, Control of spin injection by direct current in lateral spin valves, Phys. Rev. B **79**, 184415 (2009).

[6] Y. Fukuma, L. Wang, H. Idzuchi, S. Takahashi, S. Maekawa, and Y. Otani, Giant enhancement of spin accumulation and long-distance spin precession in metallic lateral spin valves, Nat. Mater. **10**, 527 (2011).

[7] E. Sagasta, Y. Omori, M. Isasa, Y. Otani, L. E. Hueso, and F. Casanova, Spin diffusion length of Permalloy using spin absorption in lateral spin valves, Appl. Phys. Lett. **111**, 082407 (2017).

[8] T. Kimura, Y. Otani, and J. Hamrle, Switching magnetization of a nanoscale ferromagnetic particle using nonlocal spin injection, Phys. Rev. Lett. **96**, 037201 (2006).

[9] L. O'Brien, M. J. Erickson, D. Spivak, H. Ambaye, R. J. Goyette, V. Lauter, P. A. Crowell, and C. Leighton, Kondo physics in non-local metallic spin transport devices, Nat. Commun. **5**, 3927 (2014).

[10] M. Takagishi, K. Yamada, H. Iwasaki, H. N. Fuke, and S. Hashimoto, Magnetoresistance ratio and resistance area design of CPP-MR film for 2–5 Tb/in^2 read sensors, IEEE Trans. Magn. **46**, 2086 (2010).

[11] M. Yamada, D. Sato, N. Yoshida, M. Sato, K. Meguro, and S. Ogawa, Scalability of spin accumulation sensor, IEEE Trans. Magn. **49**, 713 (2013).

[12] Y. K. Takahashi, S. Kasai, S. Hirayama, S. Mitani, and K. Hono, All-metallic lateral spin valves using $Co_2Fe(Ge_{0.5}Ga_{0.5})$ Heusler alloy with a large spin signal, Appl. Phys. Lett. **100**, 052405 (2012).

[13] T. Nakatani, Z. Gao, and K. Hono, Read sensor technology for ultrahigh density magnetic recording, MRS Bull. **43**, 106 (2018).

[14] S. Shirotori, S. Hashimoto, M. Takagishi, Y. Kamiguchi, and H. Iwasaki, All-metallic nonlocal spin valves using polycrystalline Co_2(FeMn)Si Heusler alloy with large output, Appl. Phys. Express **8**, 023103 (2015).

[15] B. Behin-Aein, D. Datta, S. Salahuddin, and S. Datta, Proposal for an all-spin logic device with built-in memory, Nat. Nanotechnol. **5**, 266 (2010).

[16] R. L. Stamps *et al.*, The 2014 magnetism roadmap, J. Phys. D: Appl. Phys. **47**, 333001 (2014).

[17] A. J. Wright, M. J. Erickson, D. Bromley, P. A. Crowell, C. Leighton, and L. O'Brien, Origin of the magnetic field enhancement of the spin signal in metallic nonlocal spin transport devices, Phys. Rev. B **104**, 014423 (2021).

[18] F. L. Bakker, A. Slachter, J.-P. Adam, and B. J. van Wees, Interplay of Peltier and Seebeck effects in nanoscale nonlocal spin valves, Phys. Rev. Lett. **105**, 136601 (2010).

[19] S. Kasai, S. Hirayama, Y. K. Takahashi, S. Mitani, K. Hono, H. Adachi, J. Ieda, and S. Maekawa, Thermal engineering of non-local resistance in lateral spin valves, Appl. Phys. Lett. **104**, 1 (2014).

[20] R. K. Bennet, A. Hojem, and B. L. Zink, Thermal gradients and anomalous Nernst effects in membrane-supported nonlocal spin valves, Phys. Rev. B **100**, 104404 (2019).

[21] K. S. Das, F. K. Dejene, B. J. van Wees, and I. J. Vera-Marun, Anisotropic Hanle line shape via magnetothermoelectric phenomena, Phys. Rev. B **94**, 180403(R) (2016).

[22] S. Takahashi and S. Maekawa, Spin injection and detection in magnetic nanostructures, Phys. Rev. B **67**, 052409 (2003).

[23] M. Johnson and R. H. Silsbee, Calculation of nonlocal baseline resistance in a quasi-one-dimensional wire, Phys. Rev. B **76**, 153107 (2007).

[24] B. L. Zink, Thermal effects in spintronic materials and devices: An experimentalist's guide, J. Magn. Magn. Mater. **564**, 170120 (2022).

[25] A. Slachter, F. L. Bakker, and B. J. van Wees, Anomalous Nernst and anisotropic magnetoresistive heating in a lateral spin valve, Phys. Rev. B **84**, 020412(R) (2011).

[26] S. Hu and T. Kimura, Anomalous Nernst-Ettingshausen effect in nonlocal spin valve measurement under high-bias current injection, Phys. Rev. B **87**, 014424 (2013).

[27] A. Hojem, D. Wesenberg, and B. L. Zink, Thermal spin injection and interface insensitivity in permalloy/aluminum metallic nonlocal spin valves, Phys. Rev. B **94**, 024426 (2016).

[28] A. Vedyayev, N. Ryzhanova, N. Strelkov, T. Andrianov, A. Lobachev, and B. Dieny, Nonlocal signal and noise in T-shaped lateral spin-valve structures, Phys. Rev. Appl. **10**, 064047 (2018).

[29] A. Slachter, F. L. Bakker, J.-P. Adam, and B. J. van Wees, Thermally driven spin injection from a ferromagnet into a nonmagnetic metal, Nat. Phys. **6**, 879 (2010).

[30] A. Hoffmann and S. D. Bader, Opportunities at the frontiers of spintronics, Phys. Rev. Appl. **4**, 047001 (2015).

[31] G. Stefanou *et al.*, Scanning thermal microscopy and ballistic phonon transport in lateral spin valves, Phys. Rev. Lett. **127**, 035901 (2021).

[32] F. J. Jedema, M. V. Costache, H. B. Heersche, J. J. A. Baselmans, and B. J. van Wees, Electrical detection of spin accumulation and spin precession at room temperature in metallic spin valves, Appl. Phys. Lett. **81**, 5162 (2002).

[33] J. D. Watts, J. S. Jeong, L. O'Brien, K. A. Mkhoyan, P. A. Crowell, and C. Leighton, Room temperature spin Kondo effect and intermixing in Co/Cu non-local spin valves, Appl. Phys. Lett. **110**, 222407 (2017).

[34] Y. Ji, A. Hoffmann, J. S. Jiang, J. E. Pearson, and S. D. Bader, Non-local spin injection in lateral spin valves, J. Phys. D: Appl. Phys. **40**, 1280 (2007).

[35] M. S. Alnaes, J. Blechta, J. Hake, A. Johansson, B. Kehlet, A. Logg, C. Richardson, J. Ring, M. E. Rognes, and G. N. Wells, The FEniCS project version 1.5, Arch. Numer. Softw. **3**, 100 (2015).

[36] A. Logg, K. A. Mardal, and G. Wells, *Automated Solution of Differential Equations by the Finite Element Method: The FEniCS Book*, Lecture notes in Computational Science and Engineering (Springer Verlag, Berlin, 2012).

[37] A. Logg and G. N. Wells, DOLFIN: Automated finite element computing, ACM Trans. Math. Softw. **37**, 1 (2010).

[38] F. Völklein, H. Reith, T. W. Cornelius, M. Rauber, and R. Neumann, The experimental investigation of thermal conductivity and the Wiedemann–Franz law for single metallic nanowires, Nanotech. **20**, 325706 (2009).

[39] N. T. Eigenfeld, J. C. Gertsch, G. D. Skidmore, S. M. George, and V. M. Bright, Electrical and thermal conduction in ultra-thin freestanding atomic layer deposited W nanobridges, Nanoscale **7**, 17923 (2015).

[40] S. D. Sawtelle and M. A. Reed, Temperature-dependent thermal conductivity and suppressed Lorenz number in ultrathin gold nanowires, Phys. Rev. B **99**, 054304 (2019).

[41] S. J. Mason, D. J. Wesenberg, A. Hojem, M. Manno, C. Leighton, and B. L. Zink, Violation of the Wiedemann-Franz law through reduction of thermal conductivity in gold thin films, Phys. Rev. Mater. **4**, 065003 (2020).

[42] R. J. Gripshover, J. B. VanZytveld, and J. Bass, Thermopower of pure aluminum, Phys. Rev. **163**, 598 (1967).

[43] M. A. Hossain, S. Alaie, and M. Tehrani, Measurement of the thermoelectric power factor of films over the 10–400 K range, Rev. Sci. Instrum. **87**, 045111 (2016).

[44] F. J. Blatt, D. J. Flood, V. Rowe, P. A. Schroeder, and J. E. Cox, Magnon-drag thermopower in iron, Phys. Rev. Lett. **18**, 395 (1967).

[45] B. L. Zink, A. D. Avery, R. Sultan, D. Bassett, and M. R. Pufall, Exploring thermoelectric effects and Wiedemann–Franz violation in magnetic nanostructures via micromachined thermal platforms, Solid State Commun. **150**, 514 (2010).

[46] A. D. Avery, R. Sultan, D. Bassett, D. Wei, and B. L. Zink, Thermopower and resistivity in ferromagnetic thin films near room temperature, Phys. Rev. B **83**, 100401(R) (2011).

[47] H. Ftouni, C. Blanc, D. Tainoff, A. D. Fefferman, M. Defoort, K. J. Lulla, J. Richard, E. Collin, and O. Bourgeois, Thermal conductivity of silicon nitride membranes is not sensitive to stress, Phys. Rev. B **92**, 125439 (2015).

[48] M. Asheghi, K. Kurabayashi, R. Kasnavi, and K. E. Goodson, Thermal conduction in doped single-crystal silicon films, J. Appl. Phys. **91**, 5079 (2002).

[49] P. J. Giarratano and M. C. Jones, Deterioration of heat transfer to supercritical helium at 2·5 atmospheres, Int. J. Heat Mass Transf. **18**, 649 (1975).

[50] T. Valet and A. Fert, Theory of the perpendicular magnetoresistance in magnetic multilayers, Phys. Rev. B **48**, 7099 (1993).

[51] F. K. Dejene, J. Flipse, and B. J. van Wees, Spin-dependent Seebeck coefficients of $Ni_{80}Fe_{20}$ and Co in nanopillar spin valves, Phys. Rev. B **86**, 024436 (2012).

[52] J. Chen, X. Xu, J. Zhou, and B. Li, Interfacial thermal resistance: Past, present, and future, Rev. Mod. Phys. **94**, 025002 (2022).

[53] F. Angeles, Q. Sun, V. H. Ortiz, J. Shi, C. Li, and R. B. Wilson, Interfacial thermal transport in spin caloritronic material systems, Phys. Rev. Mater. **5**, 114403 (2021).

[54] M. E. Siemens, Q. Li, R. Yang, K. A. Nelson, E. H. Anderson, M. M. Murnane, and H. C. Kapteyn, Quasi-ballistic thermal transport from nanoscale interfaces observed using ultrafast coherent soft x-ray beams, Nat. Mater. **9**, 26 (2010).

[55] A. J. Minnich, J. A. Johnson, A. J. Schmidt, K. Esfarjani, M. S. Dresselhaus, K. A. Nelson, and G. Chen, Thermal conductivity spectroscopy technique to measure phonon mean free paths, Phys. Rev. Lett. **107**, 095901 (2011).

[56] A. J. Minnich, Determining phonon mean free paths from observations of quasiballistic thermal transport, Phys. Rev. Lett. **109**, 205901 (2012).

[57] S. J. Mason, A. Hojem, D. J. Wesenberg, A. D. Avery, and B. L. Zink, Determining absolute Seebeck coefficients from relative thermopower measurements of thin films and nanostructures, J. Appl. Phys. **127**, 085101 (2020).

[58] Y. Zhang, F. Tutt, G. N. Evans, P. Sharma, G. Haugstad, B. Kaiser, J. Ramberger, S. Bayliff, Y. Tao, M. Manno *et al.*, Crystal-chemical origins of the ultrahigh conductivity of metallic delafossites, Nat. Commun. **15**, 1399 (2024).

[59] K. H. Fischer, Thermopower of dilute magnetic alloys, in *Thermoelectricity in Metallic Conductors* (Springer Science+Business Media, New York, 1978), pp. 295–305.

[60] R. Berman and J. Kopp, The thermoelectric power of dilute gold-iron alloys, J. Phys. F Met. Phys. **1**, 457 (1971).

[61] R. Berman, J. Kopp, G. A. Slack, and C. T. Walker, Magnetic field dependence of the thermoelectric power of Au + 0.03% Fe at low temperatures, Phys. Lett. A **27**, 464 (1968).

[62] R. A. Weiner and T. M. Béal-Monod, Field-dependent thermopower of dilute magnetic alloys, Phys. Rev. B **2**, 2675 (1970).

[63] K. Maki, Thermoelectric power in dilute magnetic alloys, Prog. Theor. Phys. **41**, 586 (1969).

[64] S. J. Watzman, R. A. Duine, Y. Tserkovnyak, S. R. Boona, H. Jin, A. Prakash, Y. Zheng, and J. P. Heremans, Magnon-drag thermopower and Nernst coefficient in Fe, Co, and Ni, Phys. Rev. B **94**, 144407 (2016).

[65] A. D. Avery and B. L. Zink, Peltier cooling and onsager reciprocity in ferromagnetic thin films, Phys. Rev. Lett. **111**, 126602 (2013).